ORAL/POSTER REFERENCE: ICF100410OR

LOCAL FRACTURE PROPERTIES IN MMCS

O. Kolednik and I. Sabirov

Erich Schmid Institute of Materials Science, Austrian Academy of Sciences,
A - 8700 Leoben, Austria

ABSTRACT

The purpose of this paper is to explore the effect of the local microstructure near the crack tip on the local fracture properties of an aluminum based metal matrix composite with a varying volume fraction of alumina particles. It is investigated how parameters, such as the distance and the position of the first particle from the crack tip, the particle size, or the distance to neighbour particles, influence the local fracture initiation toughness. Furthermore, the local conditions for void initiation by either particle fracture or matrix-particle decohesion are studied. A new digital image analysis system is applied to perform a quantitative analysis of the fracture surfaces from stereo image pairs. The critical crack tip opening displacement, COD_i, and the crack tip opening displacement in the moment of void initiation, COD_{vi}, are determined as a function of the distance and the angle of the nearest alumina particles from the pre-fatigue crack front. The maximum normal stresses, $\sigma_{max,vi}$, that are necessary to initiate voids at the different individual particle locations are roughly estimated and compared. It is found that most critical are not the particles located directly in front of the crack tip but those that lie in the direction of the maximum extension of the plastic zone.

KEYWORDS

metal matrix composite, automatic fracture surface analysis, critical crack tip opening displacement, void initiation, stereophotogrammetry, local fracture toughness, microstructure

INTRODUCTION

A new automatic fracture surface analysis system has been recently developed that is capable of analyzing automatically stereo image pairs taken in the scanning electron microscope (SEM) [1,2]. Compared to a predecessor version [3,4], the system has been improved appreciably. The key part of the system is a matching algorithm which is able to find very accurately homologue, i.e. identical, points in the stereo image pair. The system generates a digital elevation model of the depicted region consisting of about 10.000 to 30.000 points. Important capabilities of the system are the automatic extraction of profile and surface roughness parameters and the determination of fractal dimensions [5], as well as the measurement of the critical crack tip opening displacement, COD_i, or the crack tip opening angle, *CTOA*, [4,6]. By this way, the fracture toughness of a material can be determined locally because COD_i is a measure of the local fracture initiation toughness, and *CTOA* a measure of the local crack propagation toughness [6].
With this system, we have now the tool to investigate how the local microstructure of a material influence its local fracture properties. In this paper, this idea is demonstrated on an aluminum based metal matrix composite (MMC) with alumina particles. It is studied how parameters, such as the distance and the position of the first particle from the crack tip, the particle size, or the distance to neighbour particles, influence the local conditions for void initiation and the fracture initiation toughness.

MATERIAL, EXPERIMENTAL PROCEDURE, AND RESULTS

The determination of global tensile and fracture properties

The material is a cast and extruded MMC with an Al-6061 matrix with Al_2O_3 particles. The chemical composition is given in Table 1. The particle volume fraction is varied: f_{Al2O3} = *10, 15,* and *20%*. The material was annealed 30 minutes at 560°C, quenched in water and aged at room temperature. Compact tension (CT) specimens with a thickness B = *12.5* mm, a width of W = *40* mm and an initial crack length of $a \approx 20$ mm were machined; the specimens had an LT crack plane orientation. Fracture mechanics tests are conducted on the pre-fatigued specimens according to the ESIS standard [7]. (In a forthcoming paper, the investigation is extended where materials with different aging conditions are studied; the influence of the global constraint of the specimen is checked by testing center cracked tension specimens, too.) The results of the tests are collected in Table 2; the fracture initiation toughness is given in terms of the J-integral, $J_{0.2/Bl}$, and in terms of the critical stress intensity, K_{IC}. In the table, the tensile testing data are also listed: the Young's modulus, E, the yield stress, σ_y, the ultimate tensile strength, σ_u, and the strain hardening coefficient, N. The values for the Al-6061 matrix material are given for comparison.

TABLE 1
CHEMICAL COMPOSITION OF THE AL 6061 ALLOY

Si	Fe	Cu	Mn	Mg	Zn	Cr	Ti
0.4÷0.8	0.7	0.15÷0.4	0.15	0.8÷1.2	0.25	0.04÷0.35	0.15

TABLE 2
GLOBAL MATERIAL PROPERTIES

% Al_2O_3	E [GPa]	σ_y [MPa]	σ_u [MPa]	N [MPa]	$J_{0.2/Bl}$ [kJ/m^2]	K_{IC} [MPa$\sqrt{m}$]	σ_0 [MPa]	d_n [1]
0	71	97	183	5.0	150	109	79	0.28
10	86	159	265	6.25	10.4	32	138	0.36
15	95	158	256	6.67	6.5	26	137	0.38
20	104	172	261	7.14	6.5	26	151	0.40

Stereophotogrammetric studies

Stereo image pairs of the midsection region are taken in the SEM by tilting the specimen. Corresponding regions on both halves of the broken fracture mechanics specimens are analyzed by our automatic fracture surface analysis system. From the digital elevation models of the corresponding regions, crack profiles are extracted perpendicular to the pre-fatigue crack front. From the crack profiles, the critical crack tip opening displacement, COD_i, and the crack tip opening in the moment of void initiation, COD_{vi}, are determined.

Figure 1 shows corresponding regions near the midsection on the two specimen halves of the specimen with f_{Al2O3} = *10 %*. The pre-fatigue region (at the midsection of the page) and the region of micro-ductile fracture can be clearly distinguished. In the SEM images, corresponding profiles are indicated. The profiles are drawn so that each crosses an alumina particle that is located close to the crack front. Sometimes the paths have a zigzag shape to find easier the corresponding path on the second specimen half.

In Figure 2a, the two corresponding profiles of Particle 10 are arranged so that the moment of fracture initiation is depicted, i.e., the first void in front of the tip coalesces with the blunted crack. COD_i is easily measured, COD_i = *16* μm. The location of Particle 10 is marked in each profile. If the upper profile is shifted vertically so that the two profiles touch at this location, we get a sketch of the crack in the moment of void initiation, Figure 2b, and the crack tip opening displacement in the moment of void initiation, COD_{vi} = *10* μm. The size of the particle is measured from the SEM images, and the polar coordinates, r and θ, of the particle center with respect to the crack tip are determined from Figure 2b. All these values are collected in Table 3, together with the data of other profiles. A few COD_i-values cannot be exactly determined; they are marked by a "?" sign.

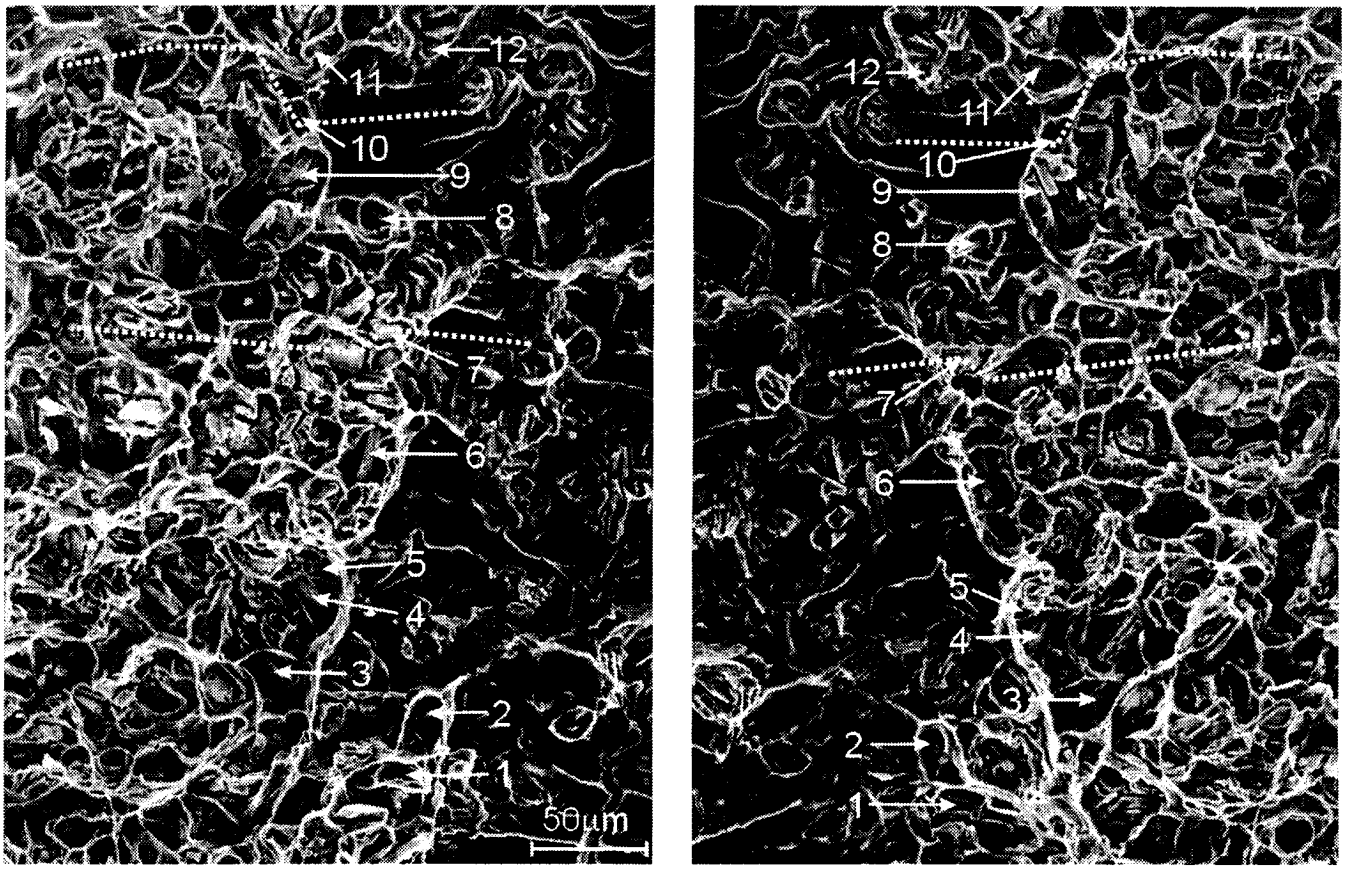

Figure 1: SEM images of corresponding midsection regions of the specimen with f_{Al2O3} = *10 %*

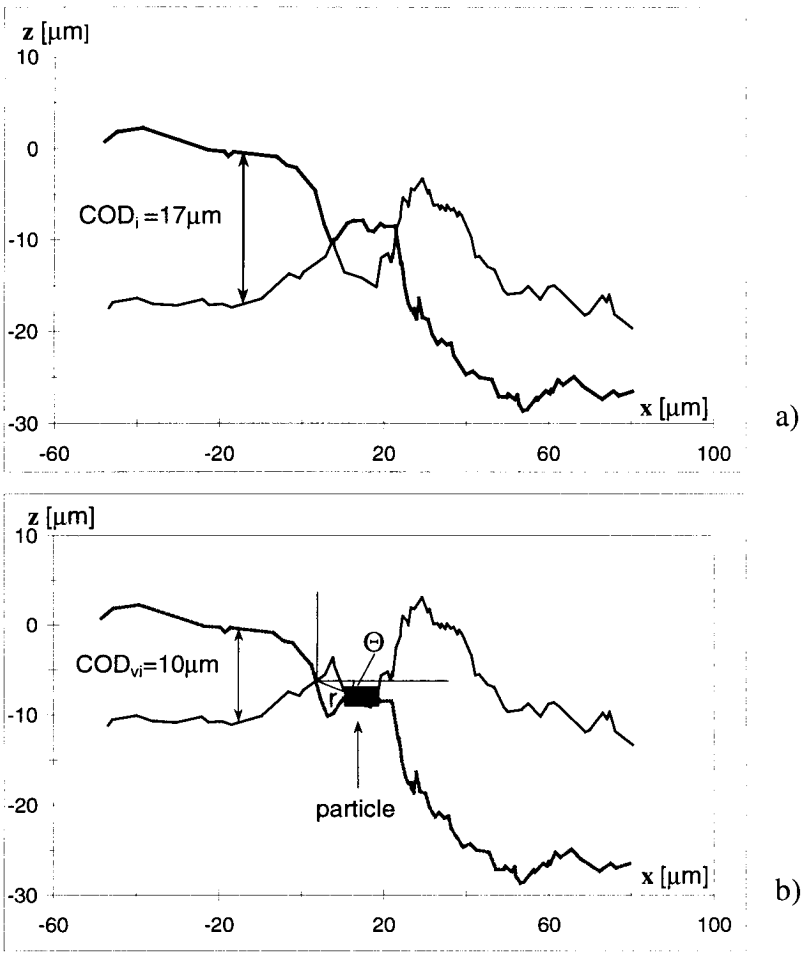

Figure 2: Crack profile through Particle 10, a) in the moment of fracture initiation, b) in the moment of void initiation at the location of the particle

TABLE 3

RESULTS OF THE STEREOPHOTOGRAMMETIC ANALYSIS FOR THE SPECIMEN WITH $f_{Al2O3} = 10\ \%$

Particle	Size [μm]	r [μm]	θ [°]	COD_{vi} [μm]	COD_i [μm]	σ^{max}_{vi} [MPa]	COD_I [μm]	Δa_I [μm]	Mecha-nism
1	3 x 12	15.6	-40	12	16.5	716	28.5	36	dec.
2	8 x 8	17.2	-31	6	6.5	644	18	17	fr.
3	12 x 3	43.2	35	7	12	571	20	65	fr.
4	20 x 9	30.5	32	7	9 ?	608	16	30	fr.
5	8 x 4	27.1	55	5	5	557	14	34	fr.
6	23 x 4	33.8	-71	≈2	13	436	19	25	fr.
7	15 x 6	30.4	-47	≈0	≈0	small	5	23	fr.
8	10 x 3	11.0	55	≈0	≈0	small	5	14	fr.
9	17 x 4	11.7	-20	6	11.5	665		>65	fr.
10	4 x 2	7.5	21	10	17	758	19.5	17	dec.
11	12 x 7	13.2	-11	9.5	16	686		>40	fr.
12	4 x 2	11.9	45	1.5	1.5 ?	549	12.5	40	fr.

Very interesting are the profiles through Particle 7, as the moments of void initiation and fracture initiation occur simultaneously at a very low value of $COD_{vi} \approx COD_i \approx 0$, Figure 3. Particle 7 fractures at a very low external loading and the crack immediately extends locally by a value of $\Delta a_I = 23$ μm. This is the first step of local crack extension. The upper profile must be shifted vertically to $COD_I = 5$ μm to produce the next step of crack extension. At a given position along the crack front, crack growth is a discontinuous process consisting of a series of local blunting and extension steps. The values of COD_k plotted against Δa_k, for $k = 1...n$, form a local crack growth resistance curve as was described in [6]. The values of the first extension step are included in Table 3.

In the region depicted in Figure 1, the crack tip opening displacement at fracture initiation varies between *0* and *17* μm, the scatter is extremely high. The mean value is $COD_i \approx (9.0 \pm 6.3)$ μm. For conventional engineering materials, such as steels, a much lower scatter of $\pm 15\%$ would be common [4,8]. On positions where COD_i is close to zero, the crack will locally extend at very low loads and stop after a crack extension, Δa_I. Against further extension, the crack will feel a much higher resistance, namely COD_I. Therefore, it is reasonable to replace at those positions COD_i by the value of COD_I, when the local average of COD_i should be compared to the global fracture initiation toughness, $J_{0.2/BI}$ or K_{IC}, measured in a fracture mechanics test. This corrected average is denoted COD_i^*. For the region of Figure 1, we get $COD_i^* \approx (10.8 \pm 4.2)$ μm.

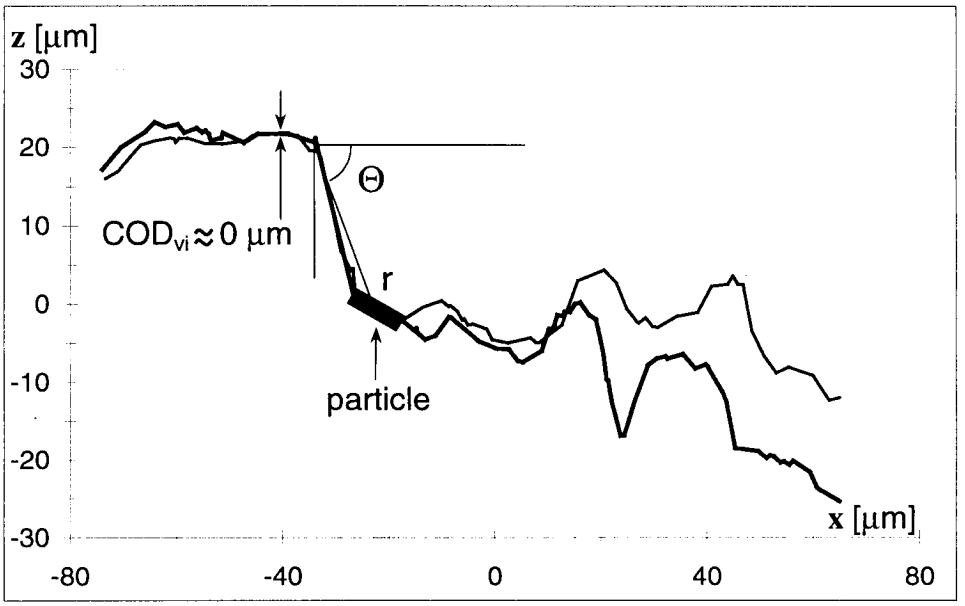

Figure 3: Crack profile through Particle 7 in the moment of void initiation; $COD_{vi} \approx COD_i \approx 0$

The mechanism of void initiation is either particle fracture, designated "fr." in the table, or matrix-particle decohesion designated "dec." For example, the broken parts of Particles 7 are found on both specimen halves, therefore particle fracture can be assumed. Void initiation by matrix/particle decohesion appears in two cases, only; most particles are fractured. The COD_{vi}-values scatter strongly, from *0* to *12* μm. No simple influence of the distance, r, between tip and particle is seen. As an example, Particle 8, with $COD_{vi} \approx 0$, is located close to the tip. In contrary, Particle 9 which has the same size and distance from the tip exhibits large values of COD_{vi} and COD_i. Very low COD_{vi}-values are also found for Particles 7 and 6 which are much more distant from the tip. It should be noticed that, with the exemption of Particle 5, the particles with a large deviation from the crack plane, i.e. a large angle θ, show very small COD_{vi}-values.

Estimate of the maximum stress at void initiation

For the individual particles, the maximum normal stress at the moment of void initiation is estimated from the solution of the HRR field which gives the stress field around a crack tip as, [9,10],

$$\sigma_{ij} = \sigma_0 \left[\frac{E\,J}{\alpha \sigma_0^{\,2} I_N\, r} \right]^{1/(N+1)} \tilde{\sigma}_{ij}(N,\Theta) \tag{1}$$

The J-integral which determines the intensity of the stress field is substituted by the relation, [11],

$$J = \frac{1}{d_N} \sigma_0\, COD \tag{2}$$

In the two equations, r and θ are the polar coordinates, I_N and d_N are dimensionless constants both depending on the strain hardening coefficient, N, and on σ_0 /E (for d_N) [11]. N, α and σ_0 determine the standard power-law work hardening behavior of the material, with $\alpha = 1$. The reference stress, σ_0, is evaluated from the tensile testing data, following the procedure outlined in Appendix 6 of the ESIS Standard [7]. The values of d_N and σ_0 are listed in Table 1.

To evaluate the stress tensor at the moment of void initiation, $\sigma_{ij,vi}$, for each individual particle, the COD_{vi}-values of Table 3 are inserted into Eqn. 2 and Eqn. 1. The values of the dimensionless function, $\sigma_{ij}(N,\theta)$, are taken from [12]. The general stress tensor $\sigma_{ij,vi}$ is transformed to get $\sigma^{max}{}_{vi}$; the results are given in Table 3. Finite element analyses have shown that, although Eqn.1 is strictly valid only for applying a small strain theory and a sharp crack, the values are valid for distances of $r \geq 2\ COD$ [13]. This condition is fulfilled for most particles. However, due to the inhomogeneity of the material the real maximum particle stresses will be higher. The $\sigma^{max}{}_{vi}$-values of Table 3 should be taken, therefore, as rough estimates that are useful only for a comparison among the different particles.

No systematic influence of the particle size on the maximum normal stress is deduced from the table. The two particles that fail by decohesion have the largest $\sigma^{max}{}_{vi}$-values. $\sigma^{max}{}_{vi}$ does not seem to be the decisive parameter, as some particles, i.e., those located at high angle θ, fail at very low maximum normal stresses.

Comparison of the different specimens

For the specimen with f_{Al2O3} = *10* %, a second region, where the SEM images are taken at a higher magnification, is analyzed in a similar way. In total, 16 near-tip alumina particles are considered. In Table 4, the average values of COD_{vi}, COD_i, and $\sigma^{max}{}_{vi}$ are collected. For the other specimens, similar analyses are performed. In the specimen with f_{Al2O3} = *15* %, 14 particles are analyzed. 3 particles had a $COD_{vi} \leq 1$ μm. In the specimen with f_{Al2O3} = *20* %, 10 particles are analyzed; 5 particles had a $COD_{vi} \leq 1$ μm. The averaged results of these specimens also listed in Table 4.

DISCUSSION

It is plausible that plastic straining induce high stresses in the particle because of the misfit strains. It can be, therefore, assumed that for void initiation the plastic strain at the position of a particle must exceed a critical value [14]. For plane strain conditions which prevail in the specimen midsection, the plastic zone has a

TABLE 4

CONDITIONS FOR VOID AND FRACTURE INITIATION AT ALUMINA PARTICLES NEAR THE CRACK FRONT (AVERAGE VALUES)

% Al_2O_3	COD_{vi} [μm]	COD_i [μm]	COD_i^* [μm]	σ^{max}_{vi} [MPa]
10	5.5	10.7	12	546
15	4.4	6.4	8.0	442
20	1.5	6.1	6.1	324

maximum extension at an angle of about $\theta = 70°$ with respect to the crack plane. In that direction, the plastic zone size is by a factor 4.4 larger than directly in the crack plane, [15],

$$\omega_{70} = 0.157 \frac{K^2}{\sigma_y^{\,2}} \approx 0.16 \frac{J E}{\sigma_y^{\,2}} \approx \frac{0.16}{d_N} \frac{E \sigma_o COD}{\sigma_y^{\,2}} \tag{3}$$

This explains that most critical are not the particles located directly in front of the crack tip but those that lie in the direction of the maximum extension of the plastic zone. Even for a very low COD of 0.5 μm, the maximum extension of the plastic zone becomes already very large compared to the distance to the nearest particle: $\omega_{70} \approx 104$ μm (for the specimen with $f_{Al2O3} = 10$ %). Void initiation is induced due to the plastic strain, mostly by particle fracture, and the crack growth is initiated by the formation and failure of a shear band from the crack tip to the pre-crack.

For higher particle volume fractions, the plastic zone size decreases slightly because of the increased flow stress; however, this is more than compensated by the decreased distance of the tip to the next particle in a location favorable for void initiation, Therefore, more and more particles fracture at a very low loading, as has been found in the analysis, and the average values of COD_{vi}, COD_i, and σ^{max}_{vi} (which is the hypothetical maximum normal stress for a homogeneous material) decrease.

ACKNOWLEDGEMENTS

The authors acknowledge gratefully the financial support of this work by the Austrian Fonds zur Förderung der wissenschaftlichen Forschung under the project number P14333-PHY.

REFERENCES

1 Scherer, S., Werth, P., Pinz, A., Tatschl, A. and Kolednik, O. (1999) In: *Electron Microscopy and Analysis 1999,* pp. 107-110, Kiely, C.J. (Ed.). Institute of Physics Publishing, Bristol, U.K.

2 Scherer, S. and Kolednik, O. (2001) *Microscopy and Analysis* 70, in press.

3 Stampfl, J., Scherer, S., Gruber, M. and Kolednik, O. (1996) *Appl. Physics* A63, 341.

4 Stampfl, J., Scherer, S., Berchthaler, M., Gruber, M. and Kolednik, O. (1996) *Int. J. Fracture* 78, 35.

5 Kolednik, O. and Schwarzböck, P. (2000) In: *Fracture Mechanics: Applications and Challanges, Proc. of ECF13,* Paper 1U.60., Fuentes, M., Elices, M. (Eds). Elsevier, Amsterdam.

6 Stampfl, J. and Kolednik, O. (2000) *Int. J. Fracture* 101, 321.

7 ESIS P2-92 (1992) ESIS Procedure for Determining the Fracture Behaviour of Materials. European Structural Integrity Society, Delft, The Netherlands.

8 Kolednik, O. and Stüwe, H.P. (1985) *Engng Fracture Mech.* **21,** 145.

9 Hutchinson, J.W. (1968) *J. Mech. Phys. Solids* 16, 13.

10 Rice, J.R. and Rosengren, G.F. (1968) *J. Mech. Phys. Solids* 16, 1.

11 Shih, C.F. (1981) *J. Mech. Phys. Solids* 29, 305.

12 Shih, C.F. (1983) Tables of HRR Singular Field Quantities, MRL E-147. Materials Research Laboratory, Brown University, Providence, RI, USA.

13 McMeeking, R.M. and Parks, D.M. (1979) *ASTM STP* 668, 175.

14 Thomason, P.F. (1990) Ductile Fracture of Metals. Pergamon Press, Oxford.

15 Levy, N., Marcal, P.V., Ostergren, W.J. and Rice, J.R. (1971) *Int. Journ. Fracture Mech.* 7, 143.